Moments and power corrections of longitudinal and transverse proton structure functions from lattice QCD

M. Batelaan,[1] K. U. Can,[1] A. Hannaford-Gunn,[1] R. Horsley,[2] Y. Nakamura,[3] H. Perlt,[4] P. E. L. Rakow,[5] G. Schierholz,[6] H. Stüben,[7] R. D. Young,[1] and J. M. Zanotti[1]

(QCDSF/UKQCD/CSSM Collaborations)

[1]*CSSM, Department of Physics, The University of Adelaide, Adelaide, South Australia 5005, Australia*
[2]*School of Physics and Astronomy, University of Edinburgh, Edinburgh EH9 3JZ, United Kingdom*
[3]*RIKEN Center for Computational Science, Kobe, Hyogo 650-0047, Japan*
[4]*Institut für Theoretische Physik, Universität Leipzig, 04103 Leipzig, Germany*
[5]*Theoretical Physics Division, Department of Mathematical Sciences, University of Liverpool, Liverpool L69 3BX, United Kingdom*
[6]*Deutsches Elektronen-Synchrotron DESY, Notkestraße 85, 22607 Hamburg, Germany*
[7]*Regionales Rechenzentrum, Universität Hamburg, 20146 Hamburg, Germany*

(Received 26 September 2022; revised 6 December 2022; accepted 22 February 2023; published 13 March 2023)

We present a simultaneous extraction of the moments of F_2 and F_L structure functions of the proton for a range of photon virtuality, Q^2. This is achieved by computing the forward Compton amplitude on the lattice utilizing the second-order Feynman-Hellmann theorem. Our calculations are performed on configurations with two different lattice spacings and volumes, all at the $SU(3)$ symmetric point. We find the moments of F_2 and F_L in good agreement with experiment. Power corrections turn out to be significant. This is the first time the Q^2 dependence of the lowest moment of F_2 has been quantified.

DOI: 10.1103/PhysRevD.107.054503

I. INTRODUCTION

Nucleon structure functions are encoded by the differential cross sections for inclusive electron-proton scattering. In terms of the partonic structure of the nucleon, the deep inelastic cross sections are dominated by the transverse structure function, F_2, which hence provides the primary constraint on the parton distributions. On the other hand, the longitudinal structure function, F_L, provides important information on the QCD structure of the proton. With a perturbatively small and calculable leading-twist component [1], F_L offers a direct measure of higher-twist effects [2]. It also offers sensitivity to the low-x gluon distribution [3].

Although the small nature of the longitudinal structure function makes it more challenging to isolate, measurements by HERA [4] and Jefferson Lab [5,6] have enabled a direct extraction of several low moments of F_L across a range of Q^2 [7]. The results reveal a tension with global PDF fits [8–10] at lower Q^2 that might indicate non-negligible higher-twist effects or an increased high-x gluon distribution [7]. It is therefore highly desirable to be able to provide first-principles theoretical predictions regarding F_L, preferably at intermediate Q^2 values where the nonperturbative effects become significant. Furthermore, an improved theoretical constraint on power corrections in the structure functions generally could be particularly beneficial in global PDF analyses [10–18].

Lattice QCD simulations of the structure functions conventionally utilize the operator product expansion (OPE) approach. Lattice simulations have been successful in computing the twist-2 contributions, however the higher-twist terms mix with those of lower-twist which gives rise to complications in the renormalization procedure [19]. This setback has limited lattice QCD to investigations of the leading-twist contributions [20,21], with fewer works on twist-3 contributions [22–24].

In this work, we present a simultaneous extraction of the low moments of the nucleon structure functions F_2 and F_L from the forward Compton amplitude calculated on the lattice. This approach circumvents the operator mixing issues since the amplitude accounts for the mixing and renormalization and contains all twist contributions. Previous successful calculations of the Compton amplitude,

leading to a determination of the moments of the nucleon structure function F_1, have been reported in [25,26], and recently extended to off-forward kinematics [27].

II. COMPTON AMPLITUDE AND MOMENTS OF STRUCTURE FUNCTIONS

In order to access the structure functions, we consider the unpolarized forward Compton tensor,

$$T_{\mu\nu}(p,q) = \left(-g_{\mu\nu} + \frac{q_\mu q_\nu}{q^2}\right)\mathcal{F}_1(\omega,Q^2) + \frac{\hat{P}_\mu \hat{P}_\nu}{p\cdot q}\mathcal{F}_2(\omega,Q^2), \tag{1}$$

where q (p) is the momentum of the virtual photon (nucleon), $\hat{P}_\mu \equiv p_\mu - (p\cdot q)q_\mu/q^2$, $\omega = (2p\cdot q)/Q^2$, and $Q^2 = -q^2$. The Lorentz invariant Compton structure functions $\mathcal{F}_{1,2}$ are related to the physical structure functions $F_{1,2}$ via the optical theorem, $\mathrm{Im}\mathcal{F}_{1,2}(\omega,Q^2) = 2\pi F_{1,2}(x,Q^2)$. Making use of analyticity, crossing symmetry, and the optical theorem, the Compton structure functions satisfy the familiar dispersion relations [28],

$$\bar{\mathcal{F}}_1(\omega,Q^2) = 2\omega^2 \int_0^1 dx \frac{2xF_1(x,Q^2)}{1-x^2\omega^2 - i\epsilon}, \tag{2}$$

$$\mathcal{F}_2(\omega,Q^2) = 4\omega \int_0^1 dx \frac{F_2(x,Q^2)}{1-x^2\omega^2 - i\epsilon}, \tag{3}$$

where $\bar{\mathcal{F}}_1(\omega,Q^2) = \mathcal{F}_1(\omega,Q^2) - \mathcal{F}_1(0,Q^2)$.

The parametrization of the forward Compton amplitude in terms of F_1 and F_2 is not unique. Alternatively, we can consider a parametrization in terms of the transverse, $2xF_1$, and longitudinal, F_L, structure functions [28–31]. The latter is given by [28,30],

$$F_L(x,Q^2) = \left(1 - \frac{4M_N^2}{Q^2}x^2\right)F_2(x,Q^2) - 2xF_1(x,Q^2), \tag{4}$$

which can directly be obtained from the ratio of cross sections [30,31]. Here M_N is the mass of the nucleon. As $Q^2 \to \infty$, Eq. (4) reduces to $F_L(x) \to F_2(x) - 2xF_1(x)$, which vanishes in the quark-parton model due to the familiar Callan-Gross relation. In QCD, F_L is $\mathcal{O}(\alpha_s)$ suppressed at leading twist and any power correction may be identified as higher twist.

Writing,

$$\mathcal{F}_L(\omega,Q^2) = -\mathcal{F}_1(\omega,Q^2) + \left(\frac{\omega}{2} + \frac{2M_N^2}{\omega Q^2}\right)\mathcal{F}_2(\omega,Q^2), \tag{5}$$

we can express $\bar{\mathcal{F}}_L$ by a subtracted dispersion relation in terms of F_L,

$$\bar{\mathcal{F}}_L(\omega,Q^2) = \frac{8M_N^2}{Q^2}\int_0^1 dx F_2(x,Q^2) + 2\omega^2 \int_0^1 dx \frac{F_L(x,Q^2)}{1-x^2\omega^2 - i\epsilon}, \tag{6}$$

where $\bar{\mathcal{F}}_L(\omega,Q^2) = \mathcal{F}_L(\omega,Q^2) + \mathcal{F}_1(0,Q^2)$.

We isolate the Compton structure functions from the tensor in Eq. (1). Working in Minkowski space and setting $q_3 = p_3 = 0$ we have

$$\mathcal{F}_1(\omega,Q^2) = T_{33}(p,q), \tag{7}$$

$$\mathcal{F}_2(\omega,Q^2) = \frac{\omega Q^2}{2E_N^2}[T_{00}(p,q) + T_{33}(p,q)]. \tag{8}$$

$\mathcal{F}_L$ is constructed via Eq. (5).

Expanding the integrands in Eqs. (2), (3), and (6) as a geometric series, we express the Compton structure functions as infinite sums over the Mellin moments of the inelastic structure functions,

$$\bar{\mathcal{F}}_{1,L}(\omega,Q^2) = \sum_{n=0}^{\infty} 2\omega^{2n} M_{2n}^{(1,L)}(Q^2), \tag{9}$$

$$\mathcal{F}_2(\omega,Q^2) = \sum_{n=1}^{\infty} 4\omega^{2n-1} M_{2n}^{(2)}(Q^2), \tag{10}$$

where $M_0^{(1)}(Q^2) = 0$, $2M_0^{(L)}(Q^2) = \frac{8M_N^2}{Q^2}M_2^{(2)}(Q^2)$,

$$M_{2n}^{(1)}(Q^2) = 2\int_0^1 dx x^{2n-1} F_1(x,Q^2), \tag{11}$$

$$M_{2n}^{(2,L)}(Q^2) = \int_0^1 dx x^{2n-2} F_{2,L}(x,Q^2), \tag{12}$$

for $n > 0$.

For our purposes, it is convenient to express the expansion of $\mathcal{F}_2$ in terms of the independently positive-definite moments of F_1 and F_L,

$$\frac{\mathcal{F}_2(\omega)}{\omega} = \frac{\tau}{(1+\tau\omega^2)}\sum_{n=0}^{\infty} 4\omega^{2n}\left[M_{2n}^{(1)} + M_{2n}^{(L)}\right], \tag{13}$$

where $\tau = Q^2/4M_N^2$. The intercept at $\omega = 0$ is proportional to the lowest moment of F_2, i.e. $M_2^{(2)}(Q^2)$. Higher moments are given by the appropriate combinations of the moments of F_1 and F_L.

In the following discussion, we provide the details of our procedure for extracting the moments directly from the Compton amplitude obtained in a lattice simulation.

III. THE FEYNMAN-HELLMANN APPROACH

The novel idea is to compute the Compton amplitude by means of the second-order Feynman-Hellmann theorem as derived and described in detail in [26]. Here we summarize

the procedure relevant to this work. We perturb the fermion action by the vector current,

$$S(\lambda) = S + \lambda \int d^3z (e^{i\mathbf{q}\cdot\mathbf{z}} + e^{-i\mathbf{q}\cdot\mathbf{z}}) \mathcal{J}_\mu(z), \tag{14}$$

where λ is the strength of the coupling between the quarks and the external field, $\mathcal{J}_\mu(z) = Z_V \bar{q}(z)\gamma_\mu q(z)$ is the electromagnetic current coupling to the quarks, $\mathbf{q}$ is the external momentum inserted by the current and Z_V is the renormalization constant for the local electromagnetic current, which has been determined in Ref. [32]. The perturbation is introduced on the valence quarks only, hence only quark-line connected contributions are taken into account in this work. For the perturbation of valence and sea quarks see [33].

We consider $q_3 = p_3 = 0$ and current components $\mathcal{J}_0$ and $\mathcal{J}_3$, enabling us to compute T_{00} and T_{33}. These are then given by the second-order energy shift [26],

$$\left.\frac{\partial^2 E_{N_\lambda}(\mathbf{p})}{\partial\lambda^2}\right|_{\lambda=0} = -\frac{T_{\mu\mu}(p,q) + T_{\mu\mu}(p,-q)}{2E_N(\mathbf{p})}, \tag{15}$$

where $T_{\mu\nu}$ is the Compton tensor defined in Eq. (1), $q = (0, \mathbf{q})$ is the external momentum encoded by Eq. (14), and $E_{N_\lambda}(\mathbf{p})$ is the nucleon energy at momentum $\mathbf{p}$ in the presence of a background field of strength λ. This expression is the principal relation that we use to access the Compton amplitude and hence the Compton structure functions given in Eqs. (7) and (8).

IV. SIMULATION AND ANALYSIS

Our lattice simulations are carried out on QCDSF/UKQCD-generated $2+1$-flavor gauge configurations. We utilize two ensembles with volumes $V = [32^3 \times 64, 48^3 \times 96]$, and couplings $\beta = [5.50, 5.65]$ corresponding to lattice spacings $a = [0.074(2), 0.068(3)]$ fm, respectively. The quark masses are tuned to the $SU(3)$ symmetric point where the masses of all three quark flavors are set to approximately the physical flavor-singlet mass, $\bar{m} = (2m_s + m_l)/3$ [34,35], yielding $m_\pi \approx [470, 420]$ MeV. We perform up to $\mathcal{O}(10^4)$ and $\mathcal{O}(10^3)$ measurements by employing up to six and three sources on the $32^3 \times 64$ and $48^3 \times 96$ ensembles of size 1764 and 537 configurations, respectively.

We follow the procedure laid out in Ref. [26] to calculate the energy shifts and extract the Compton amplitude. The calculations are done for several values of $\mathbf{q}$. Multiple values of ω are accessed by varying the nucleon momentum $\mathbf{p}$ for a fixed $\mathbf{q}$. A list of ω values used in the analysis is provided in Appendix A.

By attaching the current selectively to the u and d quarks, respectively, we obtain the flavor-diagonal contributions uu and dd corresponding to a handbag diagram at leading twist, and the mixed-flavor piece, ud, which is purely higher-twist, corresponding to a cat's ears diagram.[1] We construct the ratios,

$$\mathcal{R}^{qq}_\lambda(\mathbf{p},t) \equiv \frac{G^{(2)}_{+\lambda}(\mathbf{p},t) G^{(2)}_{-\lambda}(\mathbf{p},t)}{(G^{(2)}(\mathbf{p},t))^2} \xrightarrow{t\gg 0} A^{qq}_\lambda e^{-2\Delta E^{qq}_{N_\lambda}(\mathbf{p})t}, \tag{16}$$

$$\mathcal{R}^{qq'}_\lambda(\mathbf{p},t) \equiv \frac{G^{(2)}_{+\lambda,+\lambda}(\mathbf{p},t) G^{(2)}_{-\lambda,-\lambda}(\mathbf{p},t)}{G^{(2)}_{+\lambda,-\lambda}(\mathbf{p},t) G^{(2)}_{-\lambda,+\lambda}(\mathbf{p},t)} \xrightarrow{t\gg 0} A^{qq'}_\lambda e^{-4\Delta E^{qq'}_{N_\lambda}(\mathbf{p})t}, \tag{17}$$

in order to extract the second-order energy shifts for the flavor-diagonal ($qq = uu, dd$) and mixed-flavor ($qq' = ud$) pieces, respectively. Here, $G^{(2)}_\lambda$ denote the perturbed two-point correlation functions in the presence of the external field with the coupling strength λ. In order to calculate the ud piece as in Eq. (17), we need to consider the interference of two currents. Therefore, we compute the perturbed correlators, $G^{(2)}_{\lambda_1,\lambda_2}$, by including an additional current term in Eq. (14) with the same coupling strength in magnitude, $|\lambda_1| = |\lambda_2| = |\lambda|$ in close analogy to the off-forward case [27]. These ratios isolate the energy shifts ($\Delta E^{(qq,qq')}_{N_\lambda}(\mathbf{p})$) only at even orders of λ.

We proceed with established spectroscopy methods to extract the energy shifts from the ratios defined in Eqs. (16) and (17). Fit windows are determined following a covariance-matrix based χ^2 analysis. We perform correlated, one-exponential fits to a range of fit windows that contain at least four time slices and pick the one with the best χ^2 per degree of freedom, i.e. $\chi^2_{\text{dof}} \sim 1.0$. The majority of the chosen fit windows satisfy this criteria. Any systematic error due to the choice of fit windows could be accounted for by a weighted-averaging method [36,37]. At our current precision, we find the energy shifts that are extracted via both methods to be in good agreement. Therefore, we continue with simple one-exponential fits.

We typically compute the energy shifts $\Delta E_{N_\lambda}(\mathbf{p})$, for two $|\lambda|$ values and perform polynomial fits of the form,

$$\Delta E_{N_\lambda}(\mathbf{p}) = \lambda^2 \left.\frac{\partial^2 E_{N_\lambda}(\mathbf{p})}{\partial\lambda^2}\right|_{\lambda=\mathbf{0}} + \mathcal{O}(\lambda^4), \tag{18}$$

to determine the Compton amplitude (see Ref. [26]). Choosing $|\lambda| = \mathcal{O}(10^{-2})$, higher order $\mathcal{O}(\lambda^4)$ terms are heavily suppressed. Effective mass-plot analogs for the correlator ratios and their corresponding λ-fits are shown in Appendix A.

[1] Note that we are mentioning the leading-twist diagrams for the clarity of the discussion. In reality, the Compton amplitude includes all twist contributions.

The ω dependence of the Compton structure functions is mapped by extracting the amplitude for each pair of $(\mathbf{q}, \mathbf{p})$. Subsequently, extraction of the moments from the Compton structure functions follows the methodology described in [26]. A simultaneous fit of $\bar{\mathcal{F}}_1$ [Eq. (9)] and $\mathcal{F}_2/\omega$ [Eq. (13)] is performed in a Bayesian framework to determine the first few Mellin moments of the structure functions. We truncate both series at $n = 4$ (inclusive) when determining the moments. These moments are enforced to be positive definite and monotonically decreasing. Note that the positivity bound does not hold for the ud contributions but they are constrained by $|M_{2n}^{ud}(Q^2)|^2 \leq 4M_{2n}^{uu}(Q^2)M_{2n}^{dd}(Q^2)$, since the total inclusive cross section (hence each moment) is positive for any value of the quark charges and at all kinematics. The sequences of individual uu, dd or ud moments are selected according to the standard probability distribution, $\exp(-\chi^2/2)$, where

$$\chi^2 = \sum_{\mathcal{F}} \sum_{i} \frac{[\mathcal{F}_i^{\text{model}} - \mathcal{F}^{\text{obs}}(\omega_i)]^2}{\sigma^2} \tag{19}$$

is the χ^2 function with σ^2 the diagonal elements of the full covariance matrix. Here, $\mathcal{F}$ stands for $\bar{\mathcal{F}}_1$ and $\mathcal{F}_2$, and the index i runs through all the ω values and flavor-diagonal and mixed-flavor pieces. A posterior distribution is obtained for each moment on each bootstrap sample. Then, we resample from these distributions to form a single posterior distribution for each moment to account for the correlations between the data points. Representative posterior distributions for the lowest moments are shown in Appendix B.

V. RESULTS

We show the ω dependence of the Compton structure functions along with their fit curves in Fig. 1 for a representative case of $Q^2 = 4.86$ GeV^2 calculated on the $48^3 \times 96$ ensemble. Note that a small (large) nucleon momentum $\mathbf{p}$ does not necessarily correspond to a small (large) ω. This explains the larger uncertainties of some ω values (e.g. $\omega = 0.06$, 0.35 in Fig. 1) in comparison to their neighbors (see Figs. 5 and 6 in Appendix A for a comparison of $\omega = 0.06$ to $\omega = 0.18$).

We keep terms up to $\mathcal{O}(\omega^8)$ in the fit polynomials Eqs. (9) and (13). The lowest two moments are insensitive to the addition of higher order terms (see Appendix B). The lowest moments of the structure functions F_2 and F_L obtained from the $32^3 \times 64$ and $48^3 \times 96$ ensembles are shown in Figs. 2 and 3 as a function of Q^2 for the proton. Note that the moments of the proton are constructed via $M_{2,p}^{(2,L)} = \frac{4}{9}M_{2,uu}^{(2,L)} + \frac{1}{9}M_{2,dd}^{(2,L)} - \frac{2}{9}M_{2,ud}^{(2,L)}$. Our F_2 moments are in good agreement with the experimental moments [38], however, we remind the reader that our results do not yet incorporate chiral, infinite volume and continuum extrapolations.

Since the Compton amplitude includes all power corrections, we can estimate the leading power correction

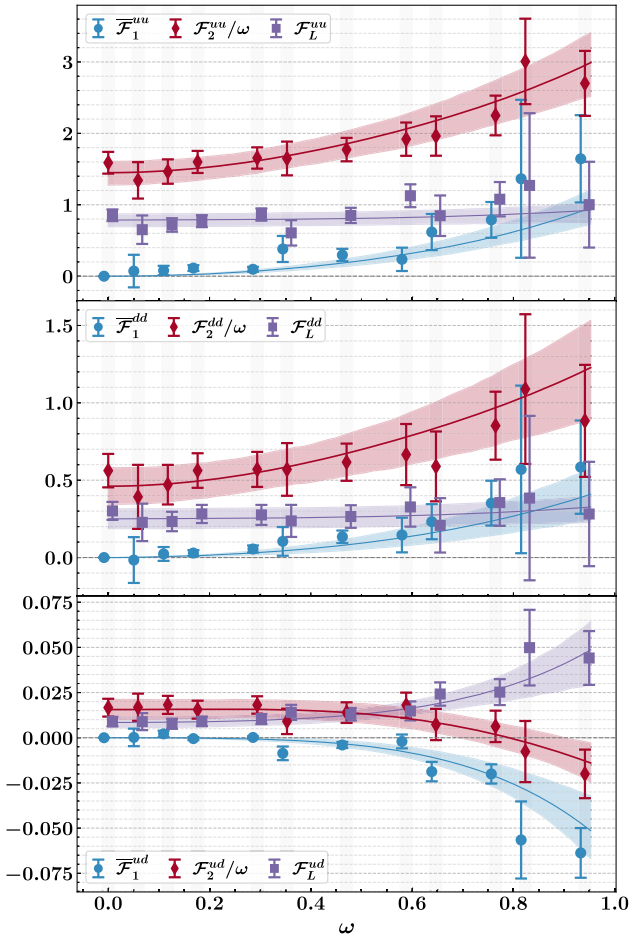

FIG. 1. ω dependence of the Compton structure functions $\bar{\mathcal{F}}_1$, $\mathcal{F}_2$, and $\bar{\mathcal{F}}_L$ at $Q^2 = 4.86$ GeV^2. We show the uu (top), dd (middle), and ud (bottom) contributions. Colored shaded bands show the fits with their 68% credible region of the highest posterior density. Points are displaced for clarity.

(i.e. twist-4) by studying the Q^2 behaviour of the moments. Higher-twist contributions are suppressed by powers of $1/Q^2$ so one expects to have sizeable contributions for intermediate to low Q^2. Their effect (at the lowest order) can be modelled by the twist expansion,

$$M_{2,h}^{(2)}(Q^2) = M_{2,h}^{(2)} + C_{2,h}^{(2)}/Q^2 + \mathcal{O}(1/Q^4), \tag{20}$$

where $h \in \{uu, dd, ud, p\}$. We utilize only the $M_2^{(2)}(Q^2)$ moments obtained on the $48^3 \times 96$ ensemble down to $Q^2 \approx 1.5$ GeV^2 to study the power corrections. We show our fit [Eq. (20)] in Fig 2. The extracted values for $M_{2,h}^{(2)}$ and $C_{2,h}^{(2)}$ are collected in Table I. We note that our results could be useful for studies investigating the power corrections in the language of infrared renormalons [39–41].

We compare the lowest (Cornwall-Norton) moment of F_L to the experimentally determined Nachtmann moments [7] in Fig. 3. While we are unable to resolve a definitive signal

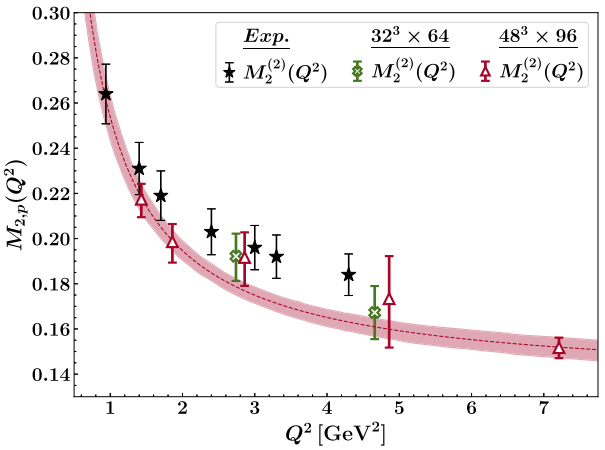

FIG. 2. Q^2 dependence of the lowest moments of F_2 for the proton. Filled stars are the experimental Cornwall-Norton moments of F_2 taken from Table I of Ref. [38]. We have assigned a 5% error to the experimental moments as indicated in Ref [38]. Red band is the fit [Eq. (20)] to the $48^3 \times 96$ data points.

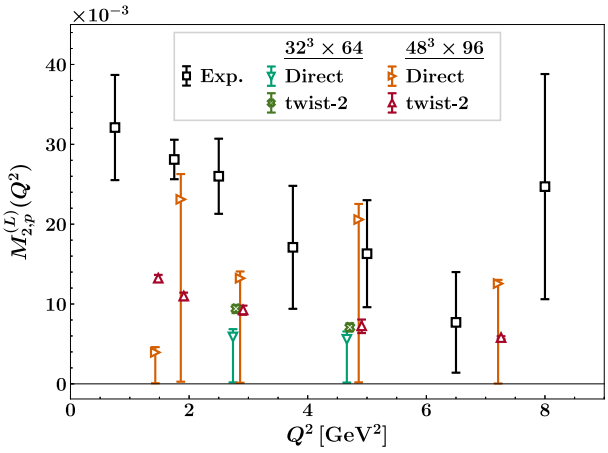

FIG. 3. Lowest moment of the proton's longitudinal structure function $M_{2,p}^{(L)}$ as a function of Q^2. We compare our results (Direct) to the experimental Nachtmann moments (open black squares) taken from [7]. Asymmetric error bars indicate that our posterior distributions are highly skewed (non-Gaussian). We also show the moments (twist-2) determined via the relation, Eq. (21), using our determination of $M_{2,p}^{(2)}$ from the current work. Twist-2 points are displaced for clarity.

for the F_L moments, we are able to set an upper bound that is compatible with the experimental moments.

It is interesting to compare $M_2^{(L)}$ determined from the relation [1],

$$M_{2,p}^{(L),\text{twist}-2}(Q^2) = \frac{4}{9\pi}\alpha_s(Q^2) M_{2,p}^{(2),\text{twist}-2}(Q^2), \quad (21)$$

where we replace the leading-twist moment on the RHS with $M_{2,p}^{(2)}(Q^2)$ from the current work as an approximation. We determine $\alpha_s(Q^2)$ at the four-loop order by running its value from the reference M_τ (tau-mass) scale that is extracted directly from τ decays [42] with $n_f = 3$ active flavors. The CRunDec package [43,44] is used to run the strong coupling constant. The effects of the number of active flavors, running from the M_Z scale as opposed to M_τ scale, and crossing the charm-quark threshold are negligible at this stage in contrast to the large uncertainties of experimental and lattice data.

TABLE I. Extracted asymptotic values of the moments and the coefficients of the power correction terms. The power corrections are quoted at the scale of the nucleon mass $Q^2 = M_N^2$.

h	$M_{2,h}^{(2)}$	$C_{2,h}^{(2)}/M_N^2$
uu	0.268(13)	0.206(24)
dd	0.146(7)	0.024(14)
ud	0.000(0)	0.007(3)
p	0.135(6)	0.091(11)

The Q^2 behavior is in good agreement with experimental points as shown in Fig. 3. With improved precision in future studies, contrasting the direct determination and twist-2 part of the lowest few moments of F_L would provide improved constraints on higher-twist effects.

VI. CONCLUSIONS

We have presented results of the lowest moments of the proton structure functions F_2 and F_L as a function of Q^2, ranging from $Q^2 \approx 1$ GeV^2 to $Q^2 \approx 7$ GeV^2. The calculations have been done at the SU(3) flavor symmetrical point. This has been possible for the first time on the lattice, due to recent advances in computing the forward Compton amplitude using the second-order Feynman-Hellmann theorem. Power corrections turn out to be significant, up to $Q^2 \approx 5$ GeV^2, and much larger than anticipated in theoretical estimates [15,40]. Already at unphysical quark masses we find good agreement with the moments extracted from experiment. However, calculations on additional ensembles that cover a range of lattice spacings and pion masses are required to fully account for systematic effects and rigorously confirm our findings. Our results are encouraging and show the potential of this approach to nucleon structure, starting from the all-encompassing Compton amplitude. The next natural step is to quantify the lattice systematics. Beyond the unpolarized structure, we are working towards extending our formalism to include the spin-dependent structure functions. Additionally, applying this method to the parity violating sector by considering weak currents is an exciting future direction.

ACKNOWLEDGMENTS

We would like to thank Wally Melnitchouk for fruitful discussions. The numerical configuration generation (using the BQCD lattice QCD program [45]) and data analysis

(using the Chroma software library [46]) was carried out on the DiRAC Blue Gene Q and Extreme Scaling (EPCC, Edinburgh, UK) and Data Intensive (Cambridge, UK) services, the GCS supercomputers JUQUEEN and JUWELS (NIC, Jülich, Germany) and resources provided by HLRN (The North-German Supercomputer Alliance), the NCI National Facility in Canberra, Australia (supported by the Australian Commonwealth Government) and the Phoenix HPC service (University of Adelaide). R. H. is supported by STFC through Grant No. ST/P000630/1. P. E. L. R. is supported in part by the STFC under Contract No. ST/G00062X/1. K. U. C., R. D. Y., and J. M. Z. are supported by the Australian Research Council Grants No. DP190100297 and No. DP220103098.

APPENDIX A: EXTRACTING THE ENERGY SHIFTS

We form the ratios defined in Eqs. (16) and (17) in order to extract the energy shifts from the perturbed correlators. The allowed $\mathbf{p}$ momenta are limited by $\mathbf{p}^2 \leq [5, 5, 5, 10, 17]$ in lattice units for $\mathbf{q} = [(3,1,0), (3,2,0), (4,2,0),$

TABLE II. Multiple ω values that we can access with several combinations of $\mathbf{p} = (p_1, p_2, p_3)$ and $\mathbf{q} = (q_1, q_2, q_3)$ in lattice units, where we have set $p_3 = q_3 = 0$. We only show the $(\mathbf{p}, \mathbf{q})$ combinations that give a positive ω. The $\omega \geq 1$ values (indicated by italics) are omitted since they lie outside the allowed ω range. The regular typeset ω values are also omitted due to their poor signal quality. We use the ω values shown in boldface only.

	$\omega = 2\mathbf{p}\cdot\mathbf{q}/Q^2$				
	$\mathbf{q}/(2\pi/L)$				
$\mathbf{p}/(2\pi/L)$	(3, 1, 0)	(3, 2, 0)	(4, 2, 0)	(5, 3, 0)	(7, 1, 0)
(0, 0, 0)	**0.0**	**0.00**	**0.0**	**0.00**	**0.00**
(0, 1, 0)	**0.2**	**0.31**	**0.2**	**0.18**	**0.04**
(0, 2, 0)	0.4	**0.62**	0.4	**0.35**	**0.08**
(0, 3, 0)	···	···	···	0.53	**0.12**
(0, 4, 0)	···	···	···	···	**0.16**
(1, 0, 0)	**0.6**	**0.46**	**0.4**	**0.29**	**0.28**
(1, 1, 0)	**0.8**	**0.77**	**0.6**	**0.47**	**0.32**
(1, 2, 0)	*1.0*	*1.08*	**0.8**	**0.65**	**0.36**
(1, 3, 0)	···	···	···	**0.82**	**0.40**
(1, 4, 0)	···	···	···	···	0.44
(1, −1, 0)	**0.4**	**0.15**	**0.2**	**0.12**	**0.24**
(1, −2, 0)	0.2	···	0.0	···	**0.20**
(−1, 2, 0)	···	**0.15**	0.0	**0.06**	···
(1, −3, 0)	···	···	···	···	**0.16**
(−1, 3, 0)	···	···	···	0.24	···
(1, −4, 0)	···	···	···	···	0.12
(2, 0, 0)	*1.2*	**0.92**	**0.8**	**0.59**	**0.56**
(2, 1, 0)	*1.4*	*1.23*	*1.0*	**0.76**	**0.60**
(2, 2, 0)	···	···	···	**0.94**	**0.64**
(2, 3, 0)	···	···	···	···	0.68
(2, −1, 0)	*1.0*	**0.62**	0.6	0.41	**0.52**
(2, −2, 0)	···	···	···	0.24	**0.48**

(Table continued)

TABLE II. *(Continued)*

	$\omega = 2\mathbf{p}\cdot\mathbf{q}/Q^2$				
	$\mathbf{q}/(2\pi/L)$				
$\mathbf{p}/(2\pi/L)$	(3, 1, 0)	(3, 2, 0)	(4, 2, 0)	(5, 3, 0)	(7, 1, 0)
(2, −3, 0)	···	···	···	···	0.44
(3, 0, 0)	···	···	···	0.88	**0.84**
(3, 1, 0)	···	···	···	*1.06*	**0.88**
(3, 2, 0)	···	···	···	···	0.92
(3, 3, 0)	···	···	···	···	0.96
(3, −1, 0)	···	···	···	0.71	**0.80**
(3, −2, 0)	···	···	···	···	0.76
(3, −3, 0)	···	···	···	···	0.72
(4, 0, 0)	···	···	···	···	*1.12*
(4, 1, 0)	···	···	···	···	*1.16*
(4, −1, 0)	···	···	···	···	*1.08*

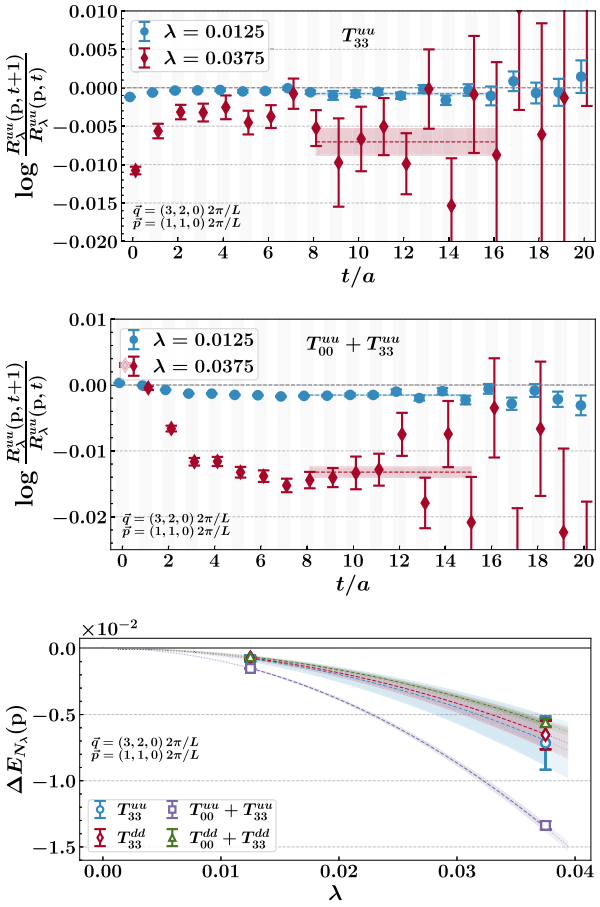

FIG. 4. Top to bottom: Effective mass plots for the correlator ratios of the amplitudes T_{33} and $T_{00} + T_{33}$, and the corresponding fits in λ-space, respectively. Shaded regions on the correlator ratio plots depict the fit windows and extracted energy shifts with their 1σ uncertainty bands. Shaded curves on the λ-fit plots indicate the fit curves and their 1σ uncertainties. We show the results for $\omega = 0.77$ ($\mathbf{p} = (1,1,0)2\pi/L$) for $\mathbf{q} = (3,2,0)2\pi/L$ obtained on the $48^3 \times 96$ ensemble.

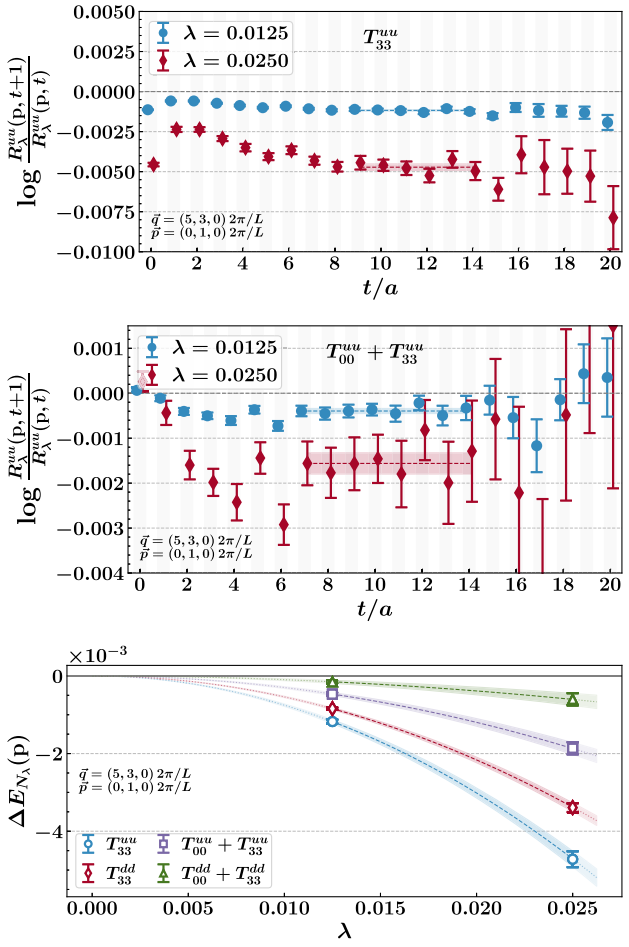

FIG. 5. Same as Fig. 4 but for $\omega = 0.18$ ($\mathbf{p} = (0,1,0)2\pi/L$) for $\mathbf{q} = (5,3,0)2\pi/L$.

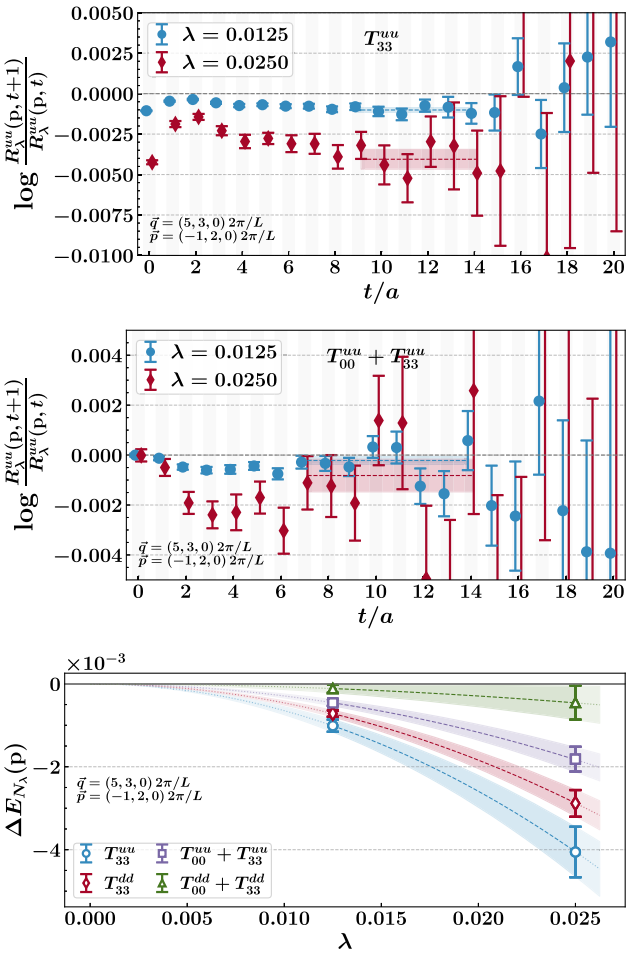

FIG. 6. Same as Fig. 4 but for $\omega = 0.06$ ($\mathbf{p} = (-1,2,0)2\pi/L$) for $\mathbf{q} = (5,3,0)2\pi/L$.

(5,3,0), $(7,1,0)]2\pi/L$, respectively. Higher $\mathbf{p}^2$ cuts introduce duplicates of ω values with worsening signal quality, thus do not expand the ω coverage any further. We tabulate the used ω values in Table II. We omit some high-$\mathbf{p}$ momenta in the analysis due to their poor S/N which hinders a reliable extraction of the ground state energy shifts. It is possible to improve the signal quality of such higher momenta correlators by employing momentum smearing techniques [47], which we plan to investigate in future work.

Effective mass plots for the correlator ratios are shown in Figs. 4–6 along with the fits performed in λ-space to extract the energy shifts for three different kinematics. We show the ratios for the uu piece only. The dd piece behaves similarly. Analogous plots for the ud piece are shown in Fig. 7. The $\mathcal{F}_1$ amplitude is isolated from T_{33} in a straightforward fashion, while the $\mathcal{F}_2/\omega$ amplitude is accessed from the $T_{00} + T_{33}$ combination up to known kinematical factors [Eq. (8)]. Top (middle) rows of Figs. 4–6 show the correlator ratios for T_{33} ($T_{00} + T_{33}$).

Fits to the energy shifts [Eq. (18)] are shown on the bottom rows of Figs. 4–6 for the uu and dd pieces of T_{33} and $T_{00} + T_{33}$ both. Since the energy shifts at different λ values are highly correlated, a χ^2-based analysis is not a reliable goodness-of-fit test. However, we confirm the suppression of the $\mathcal{O}(\lambda^4)$ term, and the absence of λ-odd terms, by including $\mathcal{O}(\lambda)$, $\mathcal{O}(\lambda^3)$, and $\mathcal{O}(\lambda^4)$ terms separately in the fit. We find that the coefficient of the linear term is consistent with zero and any residual contamination from higher-order terms has a negligible effect compared to the statistical error on the extracted amplitudes. We show the coefficient of the quadratic term [Eq. (18)] for several nucleon momenta in Fig. 8 as determined in four different ways. We either normalize the energy shifts at each λ, $\Delta E_{N_{\lambda_i}}/\lambda_i^2$, or perform fits of the form $f(\lambda) = b\lambda^2$, and $g(\lambda) = b'\lambda^2 + c\lambda^4$ that includes the quartic contamination. The data are well-described by a purely quadratic fit, $f(\lambda)$, and any quartic contamination is negligible.

Figures 5 and 6 compare the quality of the correlator ratios of $\omega = 0.06$ and $\omega = 0.18$ regarding the discussion in Sec. V. Although they lie close to each other in ω space (see Fig. 1), $\omega = 0.06$ has a larger nucleon momentum $\mathbf{p} = (-1,2,0)2\pi/L$, hence a worse S/N,

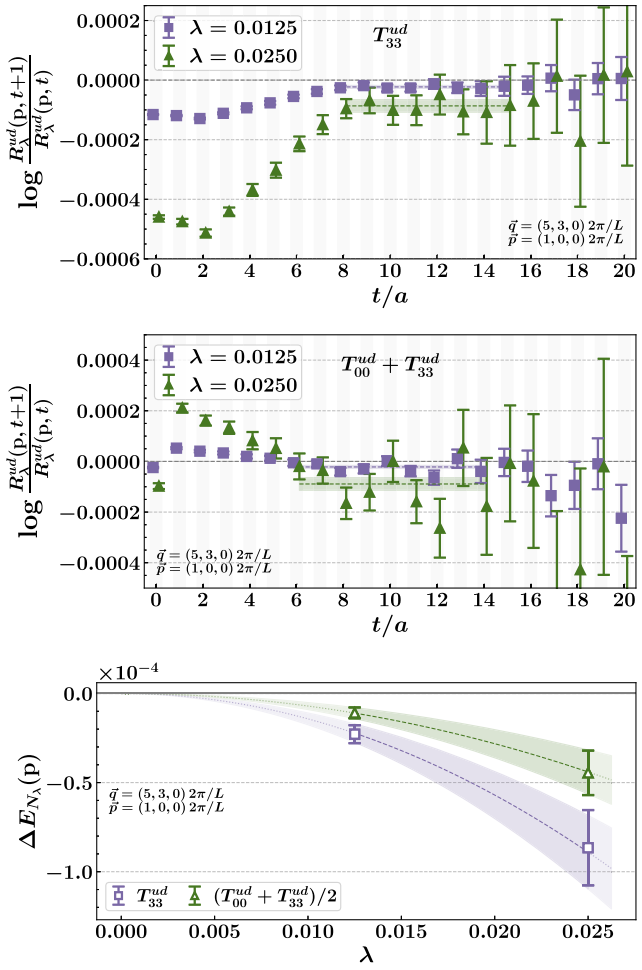

FIG. 7. Same as Fig. 4 but for the purely higher-twist *ud* piece. We show the results obtained on the $48^3 \times 96$ ensemble for the $(\mathbf{p}, \mathbf{q}) = ((1,0,0),(5,3,0))2\pi/L$ pair. Energy shifts for the $T_{00} + T_{33}$ combination have been rescaled by a factor of 0.5 on the bottom plot for clarity.

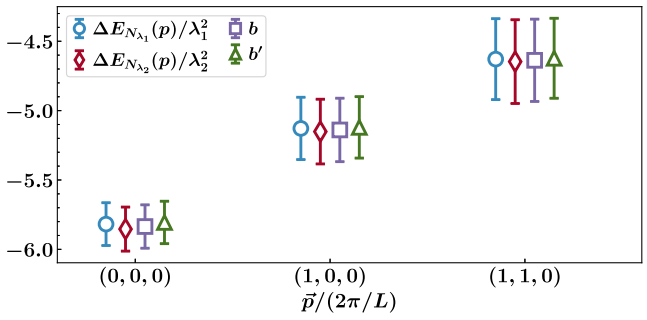

FIG. 8. The coefficient of the quadratic term in Eq. (18) determined in four different ways (see text). b and b' are the quadratic coefficients obtained from a purely quadratic, $f(\lambda) = b\lambda^2$, and a quadratic-plus-quartic, $g(\lambda) = b'\lambda^2 + c\lambda^4$, fit. We show the results for the *uu* piece obtained on the $48^3 \times 96$ ensemble at fixed $\mathbf{q} = (5,3,0)2\pi/L$.

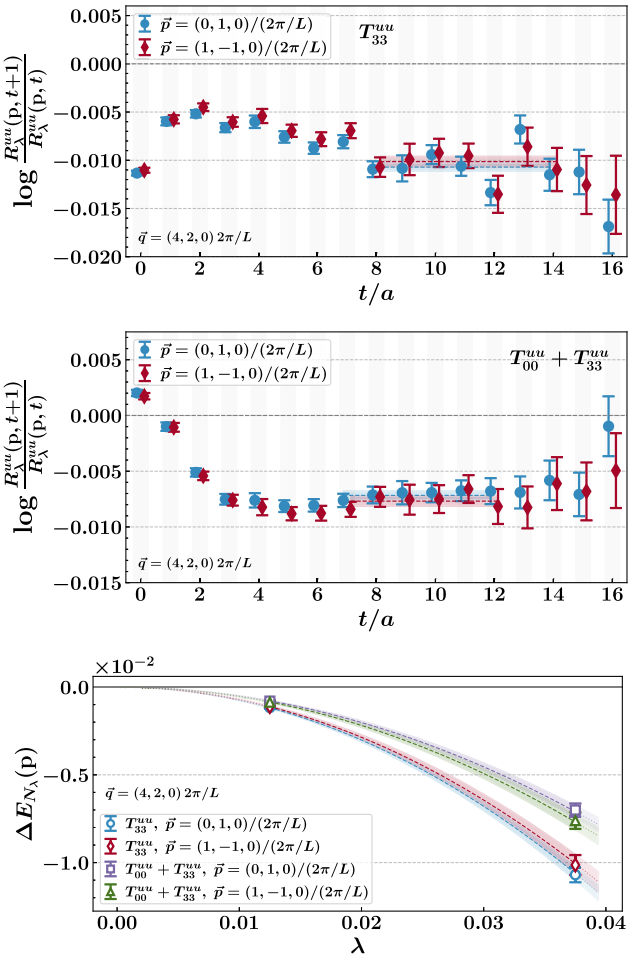

FIG. 9. Top to bottom: Correlator ratios of the amplitudes T_{33} and $T_{00} + T_{33}$ for $\lambda = 0.0375$, and the corresponding fits in λ-space, respectively, for two different $\mathbf{p}$ momenta that give $\omega = 0.2$ at fixed $\mathbf{q} = (4,2,0)2\pi/L$. See the caption of Fig. 4 for the explanation of shaded regions. We show the results for the *uu* piece obtained on the $48^3 \times 96$ ensemble.

leading to a larger uncertainty in the extracted amplitude as compared to the amplitude obtained for $\omega = 0.18$ ($\mathbf{p} = (0,1,0)2\pi/L$).

A few of the $(\mathbf{p}, \mathbf{q})$ pairs lead to the same ω for the kinematics considered in this work. We show the correlator ratios and fits to the extracted energy shifts for a representative case in Fig. 9 for the $(\mathbf{p}, \mathbf{q}) = ((0,1,0), (4,2,0))2\pi/L$ and $((1,-1,0),(4,2,0))2\pi/L$ pairs corresponding to $\omega = 0.2$. We do not find any statistically significant deviation between the amplitudes extracted from such pairs and keep all occurrences if it is not omitted due to poor signal quality.

APPENDIX B: BAYESIAN ANALYSIS

We apply the same methodology employed in Ref. [26] to extract the moments of structure functions from our Compton amplitude data. Lowest nonvanishing moments,

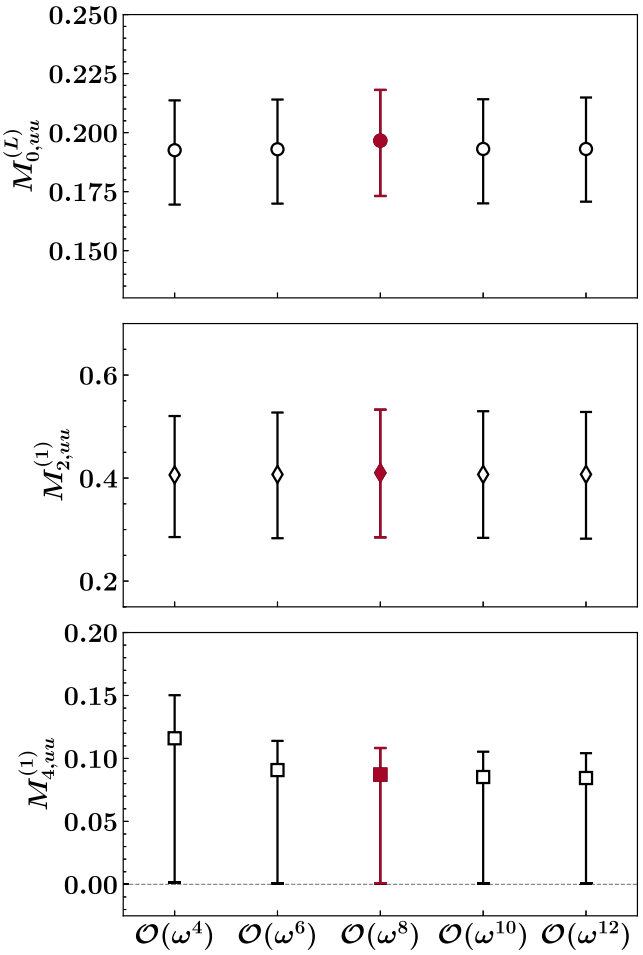

FIG. 10. Stability plots for the lowest moments obtained on the $48^3 \times 96$ ensemble at $Q^2 = 4.86$ GeV^2 for the uu contribution only. dd and ud contributions behave similarly. We show $M_0^{(L)}$ (top) that is directly proportional to the lowest moment of F_2, and the lowest two moments, $M_2^{(1)}$ (middle) and $M_4^{(1)}$ (bottom) of F_1 with respect to the number of terms kept in the fit polynomials. Color filled symbols indicate the values that we pick.

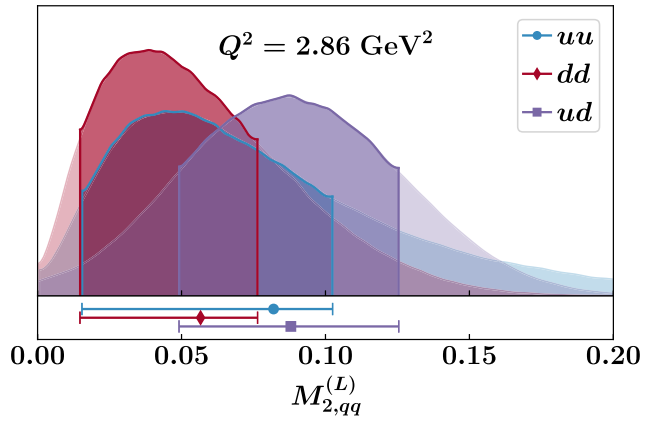

FIG. 11. Density plots of the posterior distributions for the lowest $M_2^{(L)}$ moments for uu, dd, and ud contributions. We show the results for $Q^2 = 2.86$ GeV^2 from the $48^3 \times 96$ ensemble. 68% credible regions of the highest posterior density are indicated by the darker regions on the density plot and shown on the lower panel along with the means of the distributions.

$M_2^{(1)}(Q^2)$ [Eq. (11)] and $M_{0,2}^{(L)}(Q^2)$ [Eq. (12)], are sampled from separate uniform distributions with bounds [0, 1], while the consecutive higher moments are bounded from above by their respective preceding moment, $M_{2n}^{(1,L)}(Q^2) \in [0, M_{2n-2}^{(1,L)}(Q^2)]$, for $n > 1$. Bounds for the ud moments are discussed in Sec. IV. We employ the PyMC package, a probabilistic programming library for Python [48], in our analysis.

We keep terms up to $\mathcal{O}(\omega^8)$ in the fit polynomials Eqs. (9) and (13). We find this to be the minimum required number of terms to reliably extract at least the lowest two moments from our Compton amplitude data while keeping the computational overhead low. Keeping fewer terms lead to an overestimation of the moments, while including higher-order terms have a negligible effect. We illustrate the stability of the lowest moments in Fig. 10 for a representative case.

In Fig. 11 we show the inferred posterior distributions for the $M_2^{(L)}(Q^2)$ moments at $Q^2 = 2.86$ GeV^2 for the uu, dd, and ud contributions. Although the distributions of the uu and dd pieces are skewed towards zero, a nonzero signal is obtained for both. The $M_2^{(1)}(Q^2)$ and $M_0^{(L)}(Q^2)$ distributions (not shown) have well-defined Gaussian shapes.

The lowest moments of proton F_2 and F_L shown in Figs. 2 and 3, respectively, are constructed using the individual uu, dd, and ud contributions, $M_{i,p}^{(L)} = \frac{4}{9}M_{i,uu}^{(L)} + \frac{1}{9}M_{i,dd}^{(L)} - \frac{2}{9}M_{i,ud}^{(L)}$, where $i = 0, 2$. Given that $M_{2,uu}^{(L)}$ and $M_{2,dd}^{(L)}$ are skewed towards zero and having a $M_{2,ud}^{(L)}$ contribution as significant as $M_{2,uu}^{(L)}$, the resulting $M_{2,p}^{(L)}(Q^2)$ are highly skewed towards zero making a clear exclusion of a zero value doubtful. Hence, we are only confident in setting an upper bound for the $M_{2,p}^{(L)}(Q^2)$ moments. The $M_0^{(L)}(Q^2)$ moments, on the other hand, are directly proportional to the lowest moments of F_2, i.e. the intercepts of $\mathcal{F}_2/\omega$ shown in Fig. 1, and finite.

[1] G. Altarelli and G. Martinelli, Transverse momentum of jets in electroproduction from quantum chromodynamics, Phys. Lett. **76B**, 89 (1978).

[2] S. Choi, T. Hatsuda, Y. Koike, and S. H. Lee, Twist four matrix elements of the nucleon from recent DIS data at CERN and SLAC, Phys. Lett. B **312**, 351 (1993).

[3] A. M. Cooper-Sarkar, G. Ingelman, K. R. Long, R. G. Roberts, and D. H. Saxon, Measurement of the longitudinal structure function and the small$x$ gluon density of the proton, Z. Phys. C **39**, 281 (1988).

[4] F. D. Aaron *et al.* (H1 Collaboration), Measurement of the inclusive $e^{\pm}p$ scattering cross section at high inelasticity y and of the structure function F_L, Eur. Phys. J. C **71**, 1579 (2011).

[5] Y. Liang *et al.* (Jefferson Lab Hall C E94-110 Collaboration), Measurement of $R = \sigma_L/\sigma_T$ and the separated longitudinal and transverse structure functions in the nucleon resonance region, Phys. Rev. C **105**, 065205 (2022).

[6] https://hallcweb.jlab.org/resdata/.

[7] P. Monaghan, A. Accardi, M. E. Christy, C. E. Keppel, W. Melnitchouk, and L. Zhu, Moments of the Longitudinal Proton Structure Function F_L from Global Data in the Q^2 Range 0.75–45.0 $(\mathrm{GeV}/c)^2$, Phys. Rev. Lett. **110**, 152002 (2013).

[8] A. Accardi, W. Melnitchouk, J. F. Owens, M. E. Christy, C. E. Keppel, L. Zhu, and J. G. Morfin, Uncertainties in determining parton distributions at large x, Phys. Rev. D **84**, 014008 (2011).

[9] S. Alekhin, J. Blümlein, S. Klein, and S. Moch, The 3, 4, and 5-flavor NNLO parton from deep-inelastic-scattering data and at hadron colliders, Phys. Rev. D **81**, 014032 (2010).

[10] A. D. Martin, W. J. Stirling, R. S. Thorne, and G. Watt, Parton distributions for the LHC, Eur. Phys. J. C **63**, 189 (2009).

[11] S. I. Alekhin, High twist contribution to the longitudinal structure function F_L at high x, Eur. Phys. J. C **12**, 587 (2000).

[12] A. D. Martin, R. G. Roberts, W. J. Stirling, and R. S. Thorne, Uncertainties of predictions from parton distributions. 2. Theoretical errors, Eur. Phys. J. C **35**, 325 (2004).

[13] J. Blümlein and H. Böttcher, Higher twist contributions to the structure functions $F_2^p(x, Q^2)$ and $F_2^d(x, Q^2)$ at large x and higher orders, Phys. Lett. B **662**, 336 (2008).

[14] A. Accardi, M. E. Christy, C. E. Keppel, W. Melnitchouk, P. Monaghan, J. G. Morfín, and J. F. Owens, New parton distributions from large-x and low-Q^2 data, Phys. Rev. D **81**, 034016 (2010).

[15] S. Alekhin, J. Blümlein, and S. Moch, Parton distribution functions and benchmark cross sections at NNLO, Phys. Rev. D **86**, 054009 (2012).

[16] I. Abt, A. M. Cooper-Sarkar, B. Foster, V. Myronenko, K. Wichmann, and M. Wing, Study of HERA ep data at low Q^2 and low x_{Bj} and the need for higher-twist corrections to standard perturbative QCD fits, Phys. Rev. D **94**, 034032 (2016).

[17] L. A. Harland-Lang, A. D. Martin, P. Motylinski, and R. S. Thorne, The impact of the final HERA combined data on PDFs obtained from a global fit, Eur. Phys. J. C **76**, 186 (2016).

[18] S. Alekhin, J. Blümlein, S. Moch, and R. Placakyte, Parton distribution functions, α_s, and heavy-quark masses for LHC Run II, Phys. Rev. D **96**, 014011 (2017).

[19] G. Martinelli and C. T. Sachrajda, On the difficulty of computing higher twist corrections, Nucl. Phys. **B478**, 660 (1996).

[20] H.-W. Lin *et al.*, Parton distributions and lattice QCD calculations: A community white paper, Prog. Part. Nucl. Phys. **100**, 107 (2018).

[21] M. Constantinou, L. Del Debbio, X. Ji, H.-W. Lin, K.-F. Liu, C. J. Monahan, K. Orginos, P. Petreczky, J.-W. Qiu, D. Richards, N. Sato, P. E. Shanahan, C.-P. Yuan, J.-H. Zhang, and Y. Zhao, Lattice QCD calculations of parton physics, arXiv:2202.07193.

[22] M. Göckeler, R. Horsley, D. Pleiter, P. E. L. Rakow, A. Schäfer, G. Schierholz, H. Stüben, and J. M. Zanotti, Investigation of the second moment of the nucleon's g_1 and g_2 structure functions in two-flavor lattice QCD, Phys. Rev. D **72**, 054507 (2005).

[23] S. Bhattacharya, K. Cichy, M. Constantinou, A. Metz, A. Scapellato, and F. Steffens, Insights on proton structure from lattice QCD: The twist-3 parton distribution function $g_T(x)$, Phys. Rev. D **102**, 111501(R) (2020).

[24] S. Bhattacharya, K. Cichy, M. Constantinou, A. Metz, A. Scapellato, and F. Steffens, Parton distribution functions beyond leading twist from lattice QCD: The $h_L(x)$ case, Phys. Rev. D **104**, 114510 (2021).

[25] A. J. Chambers, R. Horsley, Y. Nakamura, H. Perlt, P. E. L. Rakow, G. Schierholz, A. Schiller, K. Y. Somfleth, R. D. Young, and J. M. Zanotti (QCDSF Collaboration), Nucleon Structure Functions from Operator Product Expansion on the Lattice, Phys. Rev. Lett. **118**, 242001 (2017).

[26] K. U. Can, A. Hannaford-Gunn, R. Horsley, Y. Nakamura, H. Perlt, P. E. L. Rakow, G. Schierholz, K. Y. Somfleth, H. Stüben, R. D. Young, and J. M. Zanotti (QCDSF/UKQCD/CSSM Collaborations), Lattice QCD evaluation of the Compton amplitude employing the Feynman-Hellmann theorem, Phys. Rev. D **102**, 114505 (2020).

[27] A. Hannaford-Gunn, K. U. Can, R. Horsley, Y. Nakamura, H. Perlt, P. E. L. Rakow, G. Schierholz, H. Stüben, R. D. Young, and J. M. Zanotti (CSSM/QCDSF/UKQCD Collaborations), Generalized parton distributions from the off-forward Compton amplitude in lattice QCD, Phys. Rev. D **105**, 014502 (2022).

[28] D. Drechsel, B. Pasquini, and M. Vanderhaeghen, Dispersion relations in real and virtual Compton scattering, Phys. Rep. **378**, 99 (2003).

[29] L. N. Hand, Experimental investigation of pion electroproduction, Phys. Rev. **129**, 1834 (1963).

[30] A. Bodek, M. Breidenbach, D. L. Dubin, J. E. Elias, J. I. Friedman, H. W. Kendall, J. S. Poucher, E. M. Riordan, M. R. Sogard, D. H. Coward, and D. J. Sherden, Experimental studies of the neutron and proton electromagnetic structure functions, Phys. Rev. D **20**, 1471 (1979).

[31] W. Melnitchouk, R. Ent, and C. Keppel, Quark-hadron duality in electron scattering, Phys. Rep. **406**, 127 (2005).

[32] M. Constantinou, R. Horsley, H. Panagopoulos, H. Perlt, P. E. L. Rakow, G. Schierholz, A. Schiller, and J. M. Zanotti, Renormalization of local quark-bilinear operators for

$N_f = 3$ flavors of stout link nonperturbative clover fermions, Phys. Rev. D **91**, 014502 (2015).

[33] A. J. Chambers, R. Horsley, Y. Nakamura, H. Perlt, D. Pleiter, P. E. L. Rakow, G. Schierholz, A. Schiller, H. Stüben, R. D. Young, and J. M. Zanotti, Disconnected contributions to the spin of the nucleon, Phys. Rev. D **92**, 114517 (2015).

[34] W. Bietenholz, V. Bornyakov, N. Cundy, M. Göckeler, R. Horsley, A. D. Kennedy, W. G. Lockhart, Y. Nakamura, H. Perlt, D. Pleiter, P. E. L. Rakow, A. Schäfer, G. Schierholz, A. Schiller, H. Stüben, and J. M. Zanotti (QCDSF-UKQCD Collaboration), Tuning the strange quark mass in lattice simulations, Phys. Lett. B **690**, 436 (2010).

[35] W. Bietenholz, V. Bornyakov, M. Göckeler, R. Horsley, W. G. Lockhart, Y. Nakamura, H. Perlt, D. Pleiter, P. E. L. Rakow, G. Schierholz, A. Schiller, T. Streuer, H. Stüben, F. Winter, and J. M. Zanotti (QCDSF-UKQCD Collaborations), Flavour blindness and patterns of flavour symmetry breaking in lattice simulations of up, down and strange quarks, Phys. Rev. D **84**, 054509 (2011).

[36] S. R. Beane, W. Detmold, R. Horsley, M. Illa, M. Jafry, D. J. Murphy, Y. Nakamura, H. Perlt, P. E. L. Rakow, G. Schierholz, P. E. Shanahan, H. Stüben, M. L. Wagman, F. Winter, R. D. Young, and J. M. Zanotti (NPLQCD and QCDSF Collaborations), Charged multihadron systems in lattice QCD + QED, Phys. Rev. D **103**, 054504 (2021).

[37] M. Batelaan, R. Horsley, Y. Nakamura, H. Perlt, D. Pleiter, P. E. L. Rakow, H. Schierholz, G. Stüben, R. D. Young, and J. M. Zanotti (QCDSF-UKQCD-CSSM Collaborations), Nucleon form factors from the Feynman-Hellmann method in lattice QCD, Proc. Sci. LATTICE2021 (**2022**) 426 [arXiv:2202.01366].

[38] C. S. Armstrong, R. Ent, C. E. Keppel, S. Liuti, G. Niculescu, and I. Niculescu, Moments of the proton F_2 structure function at low Q^2, Phys. Rev. D **63**, 094008 (2001).

[39] E. Stein, M. Meyer-Hermann, L. Mankiewicz, and A. Schafer, IR-renormalon contribution to the longitudinal structure function F_L, Phys. Lett. B **376**, 177 (1996).

[40] M. Dasgupta and B. R. Webber, Power corrections and renormalons in deep inelastic structure functions, Phys. Lett. B **382**, 273 (1996).

[41] M. Beneke and V. M. Braun, Renormalons and power corrections, in *At the Frontier of Particle Physics*, edited by M. Shifman (World Scientific, Singapore, 2000), p. 1719.

[42] P. A. Baikov, K. G. Chetyrkin, and J. H. Kuhn, Order α_s^4 QCD Corrections to Z and τ Decays, Phys. Rev. Lett. **101**, 012002 (2008).

[43] K. G. Chetyrkin, J. H. Kuhn, and M. Steinhauser, RunDec: A *mathematica* package for running and decoupling of the strong coupling and quark masses, Comput. Phys. Commun. **133**, 43 (2000).

[44] F. Herren and M. Steinhauser, Version 3 of RunDec and CRunDec, Comput. Phys. Commun. **224**, 333 (2018).

[45] T. R. Haar, Y. Nakamura, and H. Stüben, An update on the BQCD hybrid Monte Carlo program, EPJ Web Conf. **175**, 14011 (2018).

[46] R. G. Edwards and B. Joó (SciDAC and LHPC and UKQCD Collaborations), The Chroma software system for lattice QCD, Nucl. Phys. B, Proc. Suppl. **140**, 832 (2005).

[47] G. S. Bali, B. Lang, B. U. Musch, and A. Schäfer (RQCD Collaboration), Novel quark smearing for hadrons with high momenta in lattice QCD, Phys. Rev. D **93**, 094515 (2016).

[48] J. Salvatier, T. V. Wiecki, and C. Fonnesbeck, Probabilistic programming in Python using PyMC3, PeerJ Comput. Sci. **2**, e55 (2016).